A NEW MULTI-SPRING ELEMENT TO SIMULATE CLT CONNECTIONS UNDER COMBINED LOADINGS

Matías F. Chacón[1], Pablo Guindos[2], Jairo Montaño[3]

ABSTRACT: A new numerical model of five uncoupled spring elements is proposed to simulate the panel-to-panel Cross-Laminated Timber (CLT) connections made of discrete fasteners. The model accurately simulates the main phenomenological effects in the translational and rotational directions of connections: asymmetrical axial gap (open/closure), in-plane and out-of-plane sliding of panels, and radial/bending stiffness/strength of fasteners. Linear/non-linear spring elements with different constitutive material models for each phenomenological effect are considered. For instance, a modified Richard–Abbott model is used for the radial/bending hysteresis of fasteners. The model is implemented in the ANSYS software through user elements and material routines. An illustrative example under different loading conditions is elaborated to show the main capabilities of the proposed model. Finally, the model is validated with two experimental monotonic in-plane CLT slab tests, where the initial/hardening stiffness, strength capacity, and failure mechanism of both specimens are correctly predicted.

KEYWORDS: CLT connection models, non-linear finite elements, phenomenological-based models, hysteretic models.

1 INTRODUCTION

1.1 OVERVIEW

Nowadays, with the arrival of new mass timber products, such as glue-laminated timber and Cross-Laminated Timber (CLT), the incorporation of efficient and innovative high-ductile connectors, and elaboration of high-precision and faster-prefabricated components, provide a viable option to build mid- to high-rise residential/non-residential buildings under a severer seismic hazard [1]. Particularly, CLT panels can be used in either floor and wall elements or as the material for the entire building.

The most critical and vulnerable part of CLT buildings is their connections, which must be designed with extreme care. Moreover, connections' mechanic capabilities (strength, stiffness, ductility, and dissipated energy) typically govern the whole structure's behaviour, particularly under seismic loads [2]. Those connections can be strengthened with an adequate layout of special straight or inclined fasteners (e.g., nails, screws), special steel parts, or slot connectors, which, together with the connection panel type (e.g., butt, half-lap, single or double surface spline) define mainly their hysteretic behaviour [3]. Several tests have been performed to characterize most of these configurations [3,4].

Complex physical effects are present in the interaction of CLT connections, such as opening/closing of panels, friction, withdrawal extraction of fasteners, large deformation and buckling of fasteners, local compression of wood, and fracture and local separation of pieces of their panels [5]. Hence, it is necessary to consider an adequate numerical model to predict the complex response of these connections and provide a more robust design process for CLT buildings.

1.2 CLT CONNECTIONS MODELING

Generally, Finite Element (FE) macro-models are used to simulate CLT connections, where each component is modelled separately, i.e., timber panels with shell elements and discrete fasteners with a set of nonlinear uniaxial or muti-directional coupled/uncoupled springs based on a mechanical and/or phenomenological material approach (e.g., walls [6] or slabs [7]). Uniaxial elements with uncoupled directional springs consider a specific model for each direction [6,8], while multi-directional coupled several directions [9]. Generally, uniaxial FEs are the most controllable and can generate a combined effect that fits well with experimental tests [10].

Phenomenological-based hysteretic models used for spring elements of CLT connections can be divided into the type of constitutive equations (e.g., algebraic [11] or first-order ordinary differential equations [12]) or in their shape (i.e., smooth [12,13] or polygonal [11,14]). The unloading/reloading paths and pinching effect are simulated in all these models with different precision levels. Moreover, some models include stiffness/strength cyclic degradation [13,14].

[1] Centro Nacional de excelencia para la industria de la Madera (CENAMAD) & Department of Structural and Geotechnical Engineering, Pontificia Universidad Católica de Chile (PUC), mfchacon@uc.cl

[2] CENAMAD & Centro UC de Innovación en Madera (CIM UC-CORMA), PUC, pguindos@ing.puc.cl

[3] CENAMAD & CIM UC-CORMA, PUC, jamontano@uc.cl

1.3 GOAL AND SCOPE

This article summarizes the main results of another recent publication by authors, which provides a new robust non-linear FE model to simulate the CLT connections made of discrete fasteners under different loading conditions. More details can be obtained in the article of Chacón *et al.*, 2023 [15]. Section 2 describes the numerical connection model, including its spring elements and material models. Moreover, an illustrative example is added to show the proposed model's capabilities. Also, Section 3 shows the results of two simulated experimental in-plane monotonic CLT slab tests with the considered FE model. Finally, the conclusions are listed in Section 4.

2 NUMERICAL CONNECTION MODEL

Five uncoupled spring elements were considered to simulate a generic discrete-fastener CLT connection. User-element and user-material FORTRAN77 subroutines of FEs and their materials were computationally implemented into the ANSYS software [16], respectively.

2.1 FINITE ELEMENTS

Two bar elements were implemented: (i) a uniaxial straight element of two nodes with one translational or rotational Degree Of Freedom (DOF) per node, called hereafter E1; and (ii) a radial 2D straight element of two nodes with two translational DOFs per node and a Lagrangean co-rotational formulation with radial strain, called hereafter RE2.

2.1.1 E1 element

This bar element has two nodes with one translational (U_x, U_y, or U_z) or one rotational DOF per node (Θ_x, Θ_y, or Θ_z), and one integration point at centroid of the element. It has a non-zero initial length l_o, and due to external forces/moments, the bar suffers a small displacement/rotation in each node $\aleph_i$ with $i \in [1,2]$. Considering a small engineering strain metric, the updated element tangent stiffness $\boldsymbol{K}_{n+1} \in \mathbb{R}^{2\times2}$ is given by

$$\boldsymbol{K}_{n+1} = v_o \frac{\partial \sigma_{n+1}}{\partial \varepsilon_{n+1}} (\boldsymbol{B} \otimes \boldsymbol{B}), \quad (1a)$$

$$\boldsymbol{B} = \frac{1}{l_o} [-1 \quad 1], \quad (1b)$$

where $v_o = Al_o$ is the initial element volume, with A being the cross-section element area, and $\frac{\partial \sigma_{n+1}}{\partial \varepsilon_{n+1}}$ is the consistent material tangent stiffness. Moreover, the updated internal force vector $\boldsymbol{F}_{\text{int}_{n+1}} \in \mathbb{R}^{2\times1}$ is expressed as

$$\boldsymbol{F}_{\text{int}_{n+1}} = v_o \boldsymbol{B}^T \sigma_{n+1}, \quad (2)$$

where σ_{n+1} is the updated material stress. Figure 1a shows two of the six cases that this element can adopt, where the U_x and Θ_y DOFs are shown. It cannot consider a zero-length element due to software restraints.
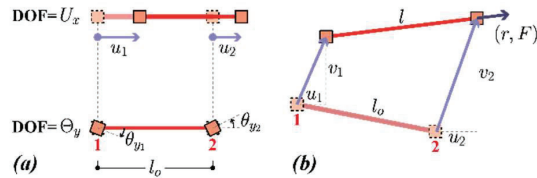

Figure 1: *Definition of the two bar finite elements implemented: (a) E1 (U_x and Θ_y DOFs cases); and (b) RE2.*

2.1.2 RE2 element

This bar element has two nodes, with two translational DOFs per node (U_x and U_y) and one integration point at the centroid of the element. Given some initial position of their nodes $\boldsymbol{x}_i = (x_i, y_i)$, with $i \in [1,2]$, due to external forces, the bar suffers a large arbitrary displacement in each node $\boldsymbol{u}_i = (u_i, v_i)$ (see Figure 1b), which elongates the bar from l_o to l length. Then, considering the Lagrangean co-rotational formulation with engineering strain metric (i.e., $\varepsilon = (l - l_o)/l_o$), the total updated tangent stiffness $\boldsymbol{K}_{n+1} \in \mathbb{R}^{4\times4}$ of this element is expressed as

$$\boldsymbol{K}_{n+1} = v_o \frac{\partial \sigma_{n+1}}{\partial \varepsilon_{n+1}} (\boldsymbol{B}_1 \otimes \boldsymbol{B}_1) + v\sigma_{n+1}(\boldsymbol{B}_2 \otimes \boldsymbol{B}_2), \quad (3)$$

where $v_o = Al_o$ and $v = Al$ are the initial/current element volume; and $\boldsymbol{B}_1$ and $\boldsymbol{B}_2$ are vectors given by

$$\boldsymbol{B}_1 = \frac{1}{l_o} [-\Delta x/l \quad -\Delta y/l \quad \Delta x/l \quad \Delta y/l], \quad (4a)$$

$$\boldsymbol{B}_2 = \frac{1}{l} [\Delta y/l \quad -\Delta x/l \quad -\Delta y/l \quad \Delta x/l], \quad (4b)$$

with $\Delta x = \Delta x_o + u_2 - u_1$, $\Delta y = \Delta y_o + v_2 - v_1$, $\Delta x_o = x_2 - x_1$, and $\Delta y_o = y_2 - y_1$. The initial/current length l_o and l can be obtained, respectively, as

$$l_o = \sqrt{\Delta x_0^2 + \Delta y_0^2}, \quad (5a)$$

$$l = \sqrt{\Delta x^2 + \Delta y^2}. \quad (5b)$$

The first term of Equation 3 represents the material tangent stiffness, while the second one the geometric stiffness. Moreover, the updated internal force vector $\boldsymbol{F}_{\text{int}_{n+1}} \in \mathbb{R}^{4\times1}$ is given by

$$\boldsymbol{F}_{\text{int}_{n+1}} = v_o \boldsymbol{B}_1^T \sigma_{n+1}. \quad (6)$$

Their element response is studied with a displacement-controlled rotation loop $\theta \in [0, 2\pi]$ and a constant stretching Δl_0, i.e., the displacement load vector $\boldsymbol{u}$ is

$$\boldsymbol{u}(\theta) = (l_o + \Delta l_0) \begin{bmatrix} \cos(\theta) \\ \sin(\theta) \end{bmatrix} - l_o \begin{bmatrix} 1 \\ 0 \end{bmatrix}. \quad (7)$$

A J_2 von Mises material model with a bi-linear isotropic hardening law is assumed. Figure 2 compares their response with the well-known two-node bar element with two translational DOFs per node. Note that only the RE2 element predicts the overall angle's response well, where a constant force and radial to the element direction independent of rotation is observed.
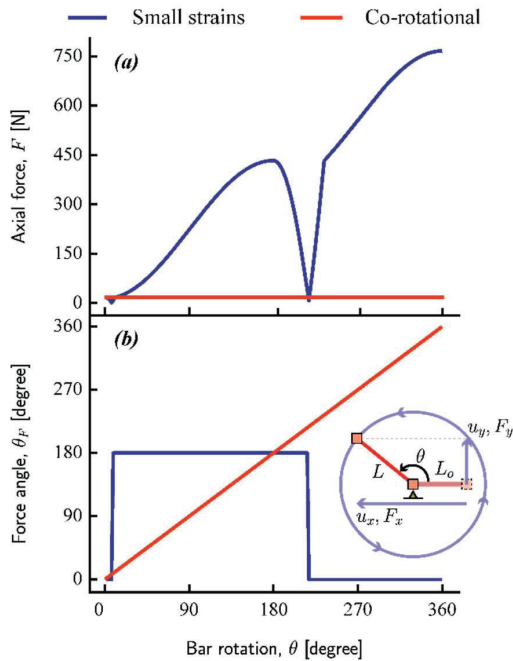
Figure 2: Comparison of the RE2 element response between small-strain and co-rotational formulations for a rotation loop $\theta \in [0,2\pi]$ with a constant stretching Δl_0: (a) force-rotation $F(\theta)$; and (b) angle force-rotation $\theta_F(\theta)$.

2.1.3 Spring elements

To simulate the discrete CLT connections, five un-coupled springs are considered: (i) axial E1 element with asymmetric tensile/compressive model to include the gap of panels; (ii) in-plane shear E1 element with linear-elastic behavior to simulate the lateral slip between panels; (iii) out-of-plane shear E1 element with linear-elastic behavior to include the vertical slip between panels; (iv) radial RE2 element with the Richard–Abbott (RA) model [17] model to add the fastener capacity; and (v) bending E1 element with the RA model to represent the out-of-plane rotation of panels. Figure 3 and Table 1 summarize these elements' main properties and functions.
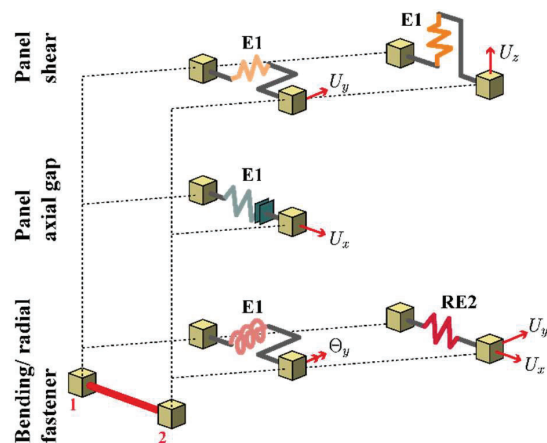

Figure 3: Spring elements to simulate a discrete CLT fastener connection. Figure extracted from Chacón et al., 2023 [15].

Table 1: Springs elements for the CLT connection model.

Id	Function	FE type	DOFs	Material
S1	Panel gap	E1	U_x	Gap
S2	In-plane shear panel	E1	U_y	Linear elastic
S3	Out-of-plane shear panel	E1	U_z	Linear elastic
S4	Radial fastener	RE2	U_x, U_y	Richard–Abbott
S5	Bending fastener	E1	Θ_y	Richard–Abbott

2.2 MATERIAL MODELS

2.2.1 Gap model

A simple and robust asymmetric model simulates the closure/opening gap of CLT panels. It is assumed the following gap force-displacement $F_g(u)$ relation

$$F_g(u) = \langle u \rangle^+ K_g^+ + \langle u \rangle^- K_g^-, \qquad (8)$$

where $K_g^\pm$ are the Positive/Negative (P/N) (opening/closure) gap stiffness, and $\langle \blacksquare \rangle^\pm$ are the P/N Macauley functions (i.e., $\langle \blacksquare \rangle^\pm = (\blacksquare \pm |\blacksquare|)/2$). Note that this relation gives a discontinuous slope at zero displacement, which can generate some convergence problems at the FE level.
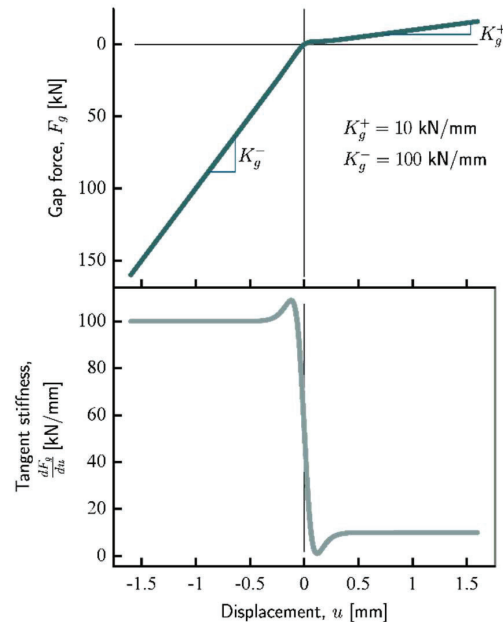

Figure 4: Response of gap model: (a) force-displacement $F_g(u)$; and (b) tangent stiffness-displacement $\frac{dF_g(u)}{du}$.

Then, Equation 8 can be rewritten in terms of some approximated smoothed (C_1-class) P/N Heaviside functions $\widetilde{H}^\pm(u)$ as

$$F_g(u) = \left(\widetilde{H}^+(u) K_g^+ + \widetilde{H}^-(u) K_g^- \right) u. \qquad (9)$$

Hence, they derivative $\frac{dF_g(u)}{du}$ can be obtained as follows

$$\frac{dF_g(u)}{du} = \sum_\aleph \left(\frac{d\widetilde{H}^\aleph(u)}{du} u + \widetilde{H}^\aleph(u) \right) K_g^\aleph, \qquad (10)$$

where symbol $\aleph$ denotes the '+' and '-' superscript, respectively. For the sake of simplicity, it is considered here the following approximated P/N Heaviside functions $\widetilde{H}^\pm(u)$

$$\widetilde{H}^\pm(u) = \frac{1}{2}[1 \pm \tanh(ku)], \qquad (11)$$

where k is an arbitrary parameter such as $\lim_{k \to \infty} \widetilde{H}^\pm(u) = H^\pm(u)$, with $H^\pm(\blacksquare)$ are the P/N stepped Heaviside functions. Figure 4 shows an illustrative example of the gap force-displacement $F_g(u)$ relation and their derivative $\frac{dF_g(u)}{du}$. Note that the slope continuity in both functions is satisfied in the overall displacement range.

2.2.2 Fastener model

A modified version by authors of the Richard–Abbott model [17] is considered to simulate the stiffness/strength fastener capacity. This model was first proposed to simulate the hysteresis of steel connections and can also adequately simulate the cyclic behaviour of timber connections. The model includes the pinching effect, symmetric/asymmetric behaviour, and low-cycle fatigue phenomena.
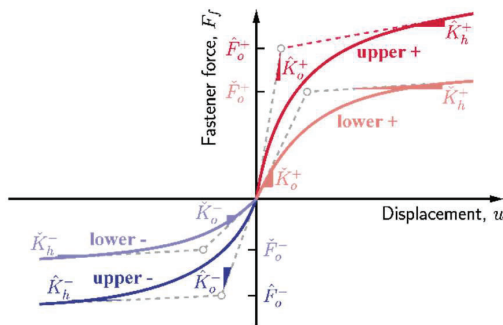

Figure 5: *Definition of parameters for the Richard-Abbott fastener model.*

First, the P/N generalized force-displacement $F_f^\pm(u)$ curves (e.g., force or moment and displacement or rotation, respectively) are stated as a combination of an upper $\hat{F}^\pm(u)$ and lower $\check{F}^\pm(u)$ P/N curves (see Figure 5), and are defined as

$$F_f^\pm(u) = f_r^\pm - \left(\frac{K_{et}^\pm}{\psi_t^\pm} + K_{ht}^\pm \right) z, \qquad \text{with} \qquad (12a)$$

$$\psi_t^\pm = \left(1 + |\phi_t^\pm|^{n_t^\pm} \right)^{1/n_t^\pm}, \qquad \phi_t^\pm = \frac{K_{et}^\pm z}{f_{1t}^\pm} \qquad (12b)$$

where $K_{et}^\pm = K_{ot}^\pm - K_{ht}^\pm$, $f_{1t}^\pm = f_{ot}^\pm + |f_r^\pm|$, $z = u_r^\pm - u$; $(u_r^\pm, f_r^\pm)$ are the P/N reversal point of curves; $f_{ot}^\pm$ are the P/N initial force; $K_{ot}^\pm$ and $K_{ht}^\pm$ are the P/N initial/hardening stiffnesses, respectively; and $n_t^\pm$ are the P/N factor that

control the shape of curves. The parameters $f_{ot}^\pm$, $K_{ot}^\pm$, $K_{ht}^\pm$, and $n_t^\pm$ are expressed as

$$K_{ot}^\pm = \check{K}_o^\pm - (\hat{K}_o^\pm + \check{K}_o^\pm)t, \qquad (13a)$$
$$K_{ht}^\pm = \check{K}_h^\pm - (\hat{K}_h^\pm + \check{K}_h^\pm)t, \qquad (13b)$$
$$f_{ot}^\pm = \check{f}_o^\pm - (\hat{f}_o^\pm + \check{f}_o^\pm)t, \qquad (13c)$$
$$n_t^\pm = \check{n}^\pm - (\hat{n}^\pm + \check{n}^\pm)t, \qquad (13d)$$

where $\hat{\blacksquare}$ and $\check{\blacksquare}$ are upper and lower parameters, respectively. The parameter $t \in [0,1]$ is a transition factor that combines the upper and lower parameters linearly and is given by

$$t = \left(\frac{v^\pm}{1+v^\pm} \right)^{t_2^\pm}, \qquad \text{with} \qquad v^\pm = \left| \frac{u - u_r^\pm}{t_3^\pm(u_{max} - u_r^\pm)} \right|^{t_1^\pm} \qquad (14)$$

where $t_3^\pm \in [0,1]$ are P/N displacement factors that control the shape of pinching curves. Note that the definition of P/N variables $v^\pm$ varies from the original RA model to give a symmetric response under symmetric displacement loads. The variable u_{max} is the maximum displacement at the loading direction, which is defined as

$$u_{max} = H^+(\zeta)r^+ + H^-(\zeta)r^-, \qquad \text{with} \qquad (15a)$$
$$r^+ = \max_{\tau \in [0,t]} (r^+(\tau), \langle u \rangle^+), \qquad (15b)$$
$$r^- = \min_{\tau \in [0,t]} (r^-(\tau), \langle u \rangle^-), \qquad (15c)$$

where $\zeta = \text{sgn}(\dot{u})$ is the loading direction, and $r^\pm$ are the P/N displacement thresholds. Note that variables $r^\pm$ grow monotonically according to obtained displacements and are independent in both directions.

Second, the model also includes a strength/stiffness degradation phenomenon (fatigue effect), where the degraded generalized force $F_\omega^\pm$ and the degraded hardening stiffness $K_{h\omega}^\pm$ are evaluated according to respective relations

$$F_\omega^\pm = (1 - \omega_f)F_f^\pm, \qquad (16a)$$
$$K_{h\omega}^\pm = (1 - \omega_k)K_h^\pm, \qquad (16b)$$

where $\omega_f \in [0,1]$ and $\omega_k \in [0,1]$ are the strength/stiffness damage variables, respectively, given by

$$\omega_f = 1 - \exp(-J_f \Upsilon), \qquad (17a)$$
$$\omega_k = 1 - \exp(-J_k \Upsilon), \qquad (17b)$$

with J_f and J_k are the strength/stiffness degraded factor, respectively. Both variables are dependent on the hysteretic dissipated energy Υ (i.e., $\Upsilon(t) = \int F(t)du$). The damage variable ω_f and ω_k does not distinguish the P/N regime, taking the accumulation in both directions. Moreover, Equations 17a-b do not require the completion of cycles to increase the damage as occurs with other proposed models [13,14].

Additionally, the choice of P/N parameters and variables $\theta^\pm$ are determined according to loading direction ζ, i.e.,

$$\theta = H^+(\zeta)\theta^+ + H^-(\zeta)\theta^-. \tag{18}$$

Finally, it is essential to note that this model considers a generalized force-displacement (or moment-rotation) relation, whereas the two material models inside of the user-implemented FEs work in the stress-strain space. Then, converting from the force-displacement to stress-strain relation is necessary to give the same FE response as the theoretical point level. Since this model has physical-based parameters, the conversion is explicit and only requires the conversion of three types of parameters: (i) P/N stiffnesses $K_o^\pm$ and $K_h^\pm$ (or $K_{\theta o}^\pm$ and $K_{\theta h}^\pm$) for the upper/lower cases; (ii) P/N strengths $F_o^\pm$ (or $M_o^\pm$) for the upper/lower cases; and (iii) energy-based strength degradation factor J_f. Then, for a force-displacement and moment-rotation relations, their respective above parameters require the following factors

$$\varphi_K = \frac{l_o}{A}, \quad \varphi_F = \frac{1}{A}, \quad \varphi_Y = l_o A, \tag{19a}$$
$$\varphi_K = \frac{l_o}{I_o}, \quad \varphi_F = \frac{1}{I_o}, \quad \varphi_Y = l_o I_o, \tag{19b}$$

where l_o is the element length, A is the cross-section element area, and I_o is the cross-section inertia of element with respect to their centroid. Note that the gap model also requires the conversion of their P/N stiffnesses $K_g^\pm$ from force-displacement to stress-strain space, which is used the factor φ_K of Equation 19a.

In summary, the model uses four quadruplets of parameters to define the upper and lower curve ($K_o^\pm$, $K_h^\pm$, $F_o^\pm$, and $n^\pm$), three pairs of parameters to state the transition parameter t ($t_2^\pm$, $t_2^\pm$, and $t_3^\pm$), and two parameters to control the fatigue (J_f and J_k). Hence, the model has a total of 24 parameters. An explicit numerical integration scheme for the updated force of this model is performed, where six state variables are considered $q = \{\zeta, Y_d, r^+, r^-, u_r, f_r\}$.

Three illustrative examples are considered to show the capabilities of this model. The first two are illustrative examples, where it is used a set of symmetrical and asymmetrical P/N parameters, respectively. In contrast, the third example is a validation of the experimental in-plane cyclic CLT connection test of Gavric *et al.* [5]. Table 2 lists all parameters considered for the three cases. Figure 6 shows the first two cases, whereas Figure 7 the third one. Four increased amplitude loading displacement cycles are applied in the first two cases (see Figure 6). The same displacement pattern as the experimental test is considered for the third case.

Table 2: Parameters for the three examples of the RA fastener model.

Parameter	Example E1	E2	E3
K_o [kN/mm]	[2, 2, 2, 2][a]	[3, 2, 3, 2]	[1, 1, 3, 3]
K_h [N/mm]	[30, 30, 10, 10]	[70, 20, 10, 10]	[220, 200, 60, 60]
F_o [kN]	[10, 10, 1, 1]	[10, 5, 3, 1]	[7, 6, -1, 2]
n [-]	[1.5, 1.5, 1.5, 1.5]	[1.5, 1.5, 1.5, 1.5]	[4, 4, 4, 4]
t_1 [-]	[10, 10][b]	[15, 15]	[40, 40]
t_2 [-]	[0.9, 0.9]	[0.9, 0.9]	[0.1, 0.1]
t_3 [-]	[0.9, 0.9]	[0.9, 0.9]	[1, 1]
J_f [-]	0	9×10^{-4}	5×10^{-7}
J_k [-]	0	1×10^{-4}	1×10^{-8}

[a] P/N upper and P/N lower values, respectively; [b] P/N values, respectively.

First, Figure 6a shows the force-displacement hysteresis using symmetrical P/N parameters, where symmetry is preserved regarding the force/stiffness of the envelopes and pinching curves. Second, Figure 6b shows the response of the second case, where a notable strength asymmetry and stiffness/strength degradation is observed. Third, a good fit in terms of envelopes and pinching paths is kept for the third case (see Figure 7a), where an error less than 1% is measured for the peak strength and respective displacement in both directions, and a coefficient of determination η_{det} (R^2) for the force history of 93.25 is calculated. Moreover, the model reproduces with considerable precision the low-cycle fatigue phenomena.
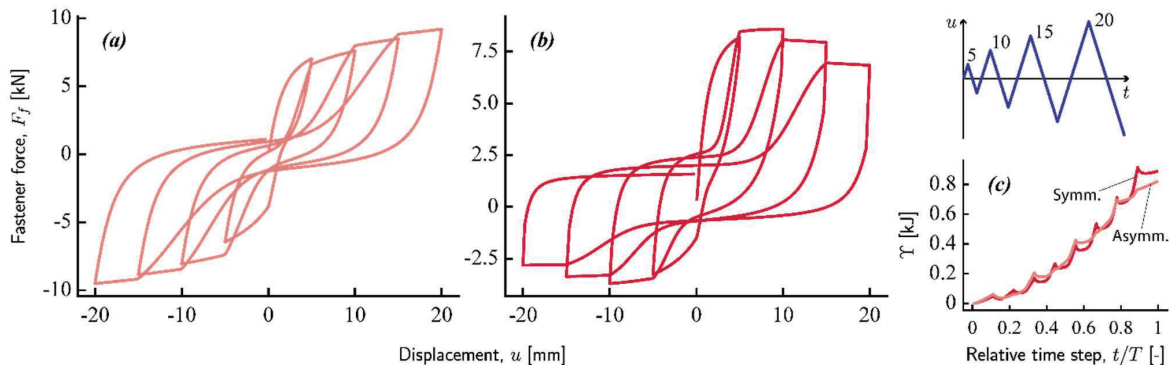

Figure 6: Force-displacement hysteresis $F_f(u)$ of the RA fastener model for two illustrative examples with different set of parameters: (a) symmetrical P/N parameters; (b) asymmetrical P/N parameters; and (c) hysteretic dissipated energy of both cases.

Moreover, Figures 6c and 7b show the history of dissipated energy $\Upsilon(t)$ for all cases. A more significant amount of energy is dissipated in the second case than in the first one one due to the incorporation of the stiffness/strength degradation factors in the model. For the third case, an excellent fit is observed concerning the experimental test, where a coefficient of determination η_{det} of 99.02 is estimated. Nevertheless, some minor differences exist, showing a moderate underestimation at 0 to 0.6, while an overestimation from 0.8 to the end is noted.
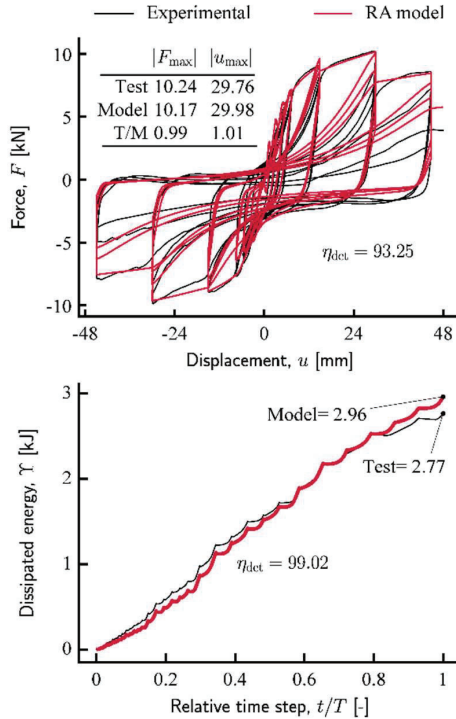

Figure 7: Third example of the RA fastener model validated with the in-plane cyclic CLT connection test of Gavric et al. 2015 [5]: (a) force-displacement $F(u)$; and (b) dissipated energy-relative time step $\Upsilon(t/T)$.

2.3 CONNECTION MODEL RESPONSE

To show the response of connection FE model under different loading conditions, an illustrative example is elaborated (see Figure 8a). Two generic square 3-layered CLT panels (t=100 mm) with a width of 1200 mm are joined with nine generic fasteners (ϕ=6 mm), equally spaced along the edge, and are loaded with different independent cyclic loads: axial, in-plane shear, and out-of-plane bending. Displacement-controlled load is applied at right edge of right panel, whereas a fixed support is considered at left edge of left panel. A gap separation of 5 mm between panels is imposed to get a more realistic response and to consider a non-zero length for the spring elements.

A Three-Dimensional (3D) FE model is generated in ANSYS, as shown in Figure 8b. On the one hand, the CLT

panels are simulated with a four-node layered-shell element SHELL181 with a linear-orthotropic material model for each lamella, whose material X-axis is oriented parallel-to-grain direction of each lamella. This element accounts for the shear distribution using the Mindlin-Reissner first-order shear-deformation theory and can adequately represent the mechanical behaviour of orthotropic plates since their stiffness depends on the loading situation. On the other hand, each fastener is simulated with the proposed set of five two-node spring elements USER300 and their materials of Sections 2.1 and 2.2, respectively.
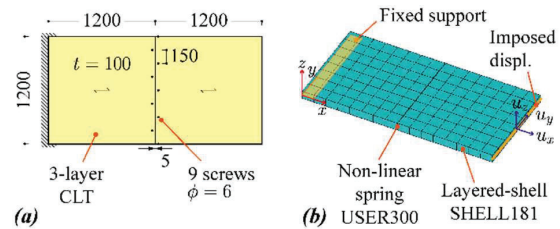

(a) 3-layer CLT   9 screws $\phi = 6$
(b) USER300   SHELL181

Figure 8: Connection model example: (a) 2D plan view of setup; and (b) 3D view of FE model. Units in millimetres.

Table 3: Material parameters for the connection model example.

Parameter	Value
CLT	
E_x, E_y, E_z [GPa]	11, 0.37, 0.37
v_{xy}, v_{xz}, v_{yz} [-]	0, 0, 0
G_{xy}, G_{xz}, G_{yz} [GPa]	0.65, 0.185[a], 0.185[a]
Radial spring (S4)	
K_o [N/mm]	[500, 500, 500, 500][b]
K_h [N/mm]	[50, 50, 20, 20]
F_o [kN]	[3, 3, 1, 1]
n [-]	[4, 4, 4, 4]
t_1 [-]	[40, 40][c]
t_2 [-]	[0.1, 0.1]
t_3 [-]	[1, 1]
J_f [-]	5×10^{-7}
J_k [-]	3×10^{-8}
Bending spring (S5)	
$K_{\theta o}$ [kN-mm/rad$\times 10^3$]	[1, 1, 1, 1][b]
$K_{\theta h}$ [kN-mm/rad]	[50, 50, 10, 10]
M_o [kN-mm]	[10, 10, 1, 1]
n [-]	[4, 4, 4, 4]
t_1 [-]	[40, 40][c]
t_2 [-]	[0.1, 0.1]
t_3 [-]	[1, 1]
J_f [-]	0
J_k [-]	3×10^{-1}
Gap spring (S1)	
K_g^+ [kN/mm]	0.13
K_g^- [kN/mm]	3.30

[a] $G_{xz} = 0.5E_x/(1 + v_{xz})$ and $G_{yz} = G_{xz}$; [b] P/N upper and P/N lower values, respectively; and [c] P/N values, respectively.

Table 3 lists the material parameters for the CLT panels and three of the five spring elements (radial, bending, and

gap). Moreover, for the two shear springs (in-plane and out-of-plane), it is assumed a linear-elastic material, where Young's modulus equal to XZ-shear modulus of CLT panels G_{xz} is considered for both springs for simplicity. Also, for the in-plane shear spring, a shear area of $A_{vy} = 5/6 A_{\text{fast}} \times 10^{-5}$, with A_{fast} is the fastener cross-section area, is assumed to simulate quasi-null in-plane friction and to avoid singularity (null pivot) at stiffness matrix. In contrast, for the out-of-plane shear spring, a shear area of $A_{vz} = 5/6 A_{\text{fast}}$ is taken because no out-of-plane slip is assumed.
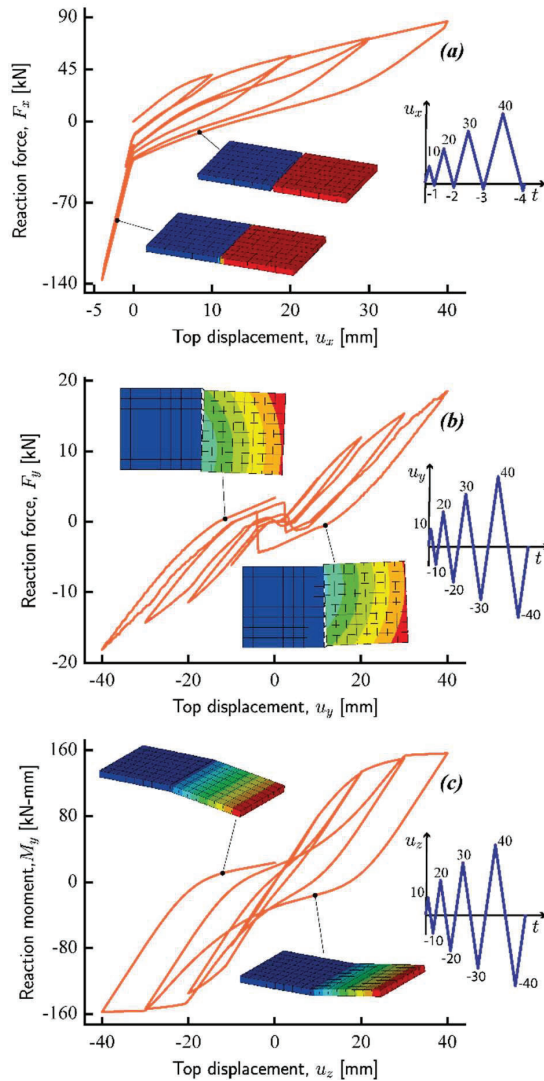

Figure 9: *Response of connection model example under different loadings conditions: (a) axial; (b) shear; and (c) bending. Figures include the displacement field of the FE model for a P/N loading condition at some unspecific time step.*

Figure 9a shows the axial reaction force-axial top displacement $F_x(u_x)$ curve of this FE model under a cyclic axial displacement load. An asymmetric displacement load pattern with four cycles of increased magnitude is considered, where positive (tensile) displacements values are larger than negative (compressive). The gap effect of panels is correctly simulated, where a cyclic behaviour with stiffness degradation and pinching is present in the tensile regime. In contrast, a marked linear-elastic behaviour is noted in the compressive one.

Figure 9b presents the in-plane reaction shear-lateral top displacement $F_y(u_y)$ relation of this FE model under a cyclic in-plane lateral displacement load. Conversely to the axial case, a symmetric P/N displacement load pattern with four cycles of increased magnitude is applied. A symmetric response is observed, with a larger amount of hardening in their envelopes, a significant pinching at the unloading/reloading paths, and an initial gap displacement of approx.—5 mm associated with the length of spring elements. Moreover, a snap-through behaviour is observed at relatively small displacements (around 5 to 10 mm), which is more pronounced at larger displacements. This phenomenon can be attributed to coupling gap/radial fastener springs. Note that this class of load test is scarce in literature (with free panel rotation) and that the shear capacity is lower than the axial one, contrary to several experimental CLT joint tests [4,5].

Figure 9c shows the bending reaction moment-vertical top displacement $M_y(u_z)$ curve of this FE model under a cyclic vertical displacement load. An identical symmetric displacement load pattern to the second case is applied vertically. A hysteretic response is observed, similar to the pure RA fastener response, like in Figure 6a, that no other coupling effects are present for this load case.

3 VALIDATION EXAMPLES

To experimentally validate the proposed numerical connection FE model, the two in-plane monotonic CLT slab test specimens of Veliz *et al.*, 2023 [18] are simulated (see Figure 10a). The first specimen, called hereafter Slab1, is composed of three 5-layered CLT panels elaborated with C24-class Chilean radiate pine (t=165 mm) and two top surface spline connections, each made of plywood (t=18.5 mm) and 11 Simpson SDWS22600 (ϕ5.6x150 mm) screws [19] alternated placed. The second specimen, called hereafter Slab2, is composed of four 3-layer CLT panels of identical wood specimen and quality (t=99 mm) and three top butt joint connections, each made of stainless-steel plate (t=3 mm) and 18 Simpson SDS25312 (ϕ6.4x89 mm) screws [19] orthogonally placed. A gap separation of 5 mm between panels was imposed initially in both specimens to avoid an undesirable compression failure between panels and neglect friction forces into the response.

Figure 10b shows the 2D plan view of both specimens and their loading setup. First, a displacement-controlled load is applied in both specimens using two actuators positioned at the middle panels (see Figure 10b). Then, a monotonic load is applied up to reach the complete failure of each slab.
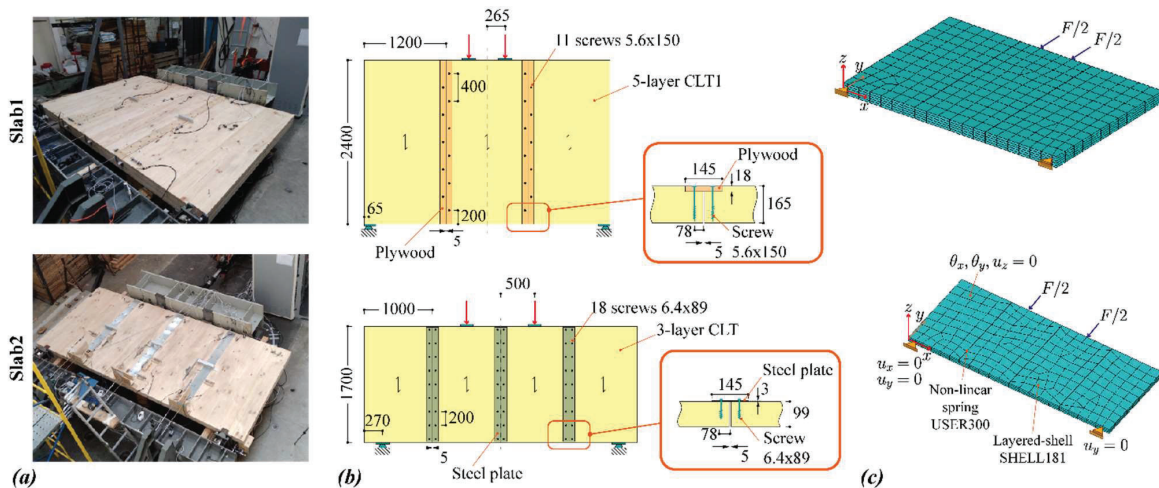
Figure 10: *In-plane monotonic CLT slabs tests of Veliz et al., 2023 [18]: (a) 3D view photograph; (b) 2D plan view of setup; and (c) 3D view of FE model. Figure extracted from Chacón et al., 2023 [15].*

Experimentally, both specimens showed a moderate ductile behaviour, with a ductility of approx. 3.5 and 2.5, respectively (see Figure 12). On the one hand, the failure mechanism of Slab1 was due to the damage of 10 screws (22 in total), which had a mixed failure mode (i.e., 4 ductile and 6 shear brittle). Moreover, fibre densification of CLT around all hole screws and penetration of almost head screws inside plywood were observed. Also, a rigid body motion of panels (without significant damage) with a moderate beam effect was observed, which generates an important shear slip of the central panel, a rotation of both lateral panels, and, consequently, a moderate lateral aperture of both connections. On the other hand, a similar failure mechanism occurred with the Slab2 due to the shear failure of 34 screws (54 in total) and tensile perpendicular-to-fibre failure at central edge panels. In addition to the fibre densification around all hole screws, the steel plates suffer a partial global buckling between each screw span and plastic deformation around screw holes. Furthermore, a more pronounced beam effect than Slab1 was viewed for this specimen due to a larger aspect ratio, where a considerable lateral aperture of connections and a less shear slip of the two central panels were noticed. Finally, note that all these observations explain why Slab2 is stiffer, stronger, and less ductile than Slab1.

Like example of Section 2.3, a 3D FE model is generated in ANSYS for each specimen, as shown in Figure 10c. On the one hand, the CLT panels are simulated with three/four-node layered-shell element SHELL181, where a linear-orthotropic material model is considered for each layer. On the other hand, each fastener is simulated with three of the five proposed spring elements and their respective materials (see Sections 2.1 and 2.2). The three springs considered are panel gap (S1), out-of-plane panel shear (S3), and radial fastener (S4). The other two springs were not required due to that was experimentally observed a significant gap separation between panels (in-plane spring S2) and a negligible out-of-plane rotations (bending fastener spring S5). Note that the out-of-plane

spring S3 was included exclusively to avoid a null pivot in the vertical direction of the element stiffness matrix. Moreover, the panel gap springs (S1) were placed only at the nearest node at the top/bottom panel edges. Table 4 lists the material parameters for the panels and two spring elements (radial and gap). Also, same spring element S3 as the example of Section 2.3 is considered here because no significant out-of-plane slip was measured. A monotonic displacement-controlled load pattern is applied equally at the two nodes where the actuators were positioned and using 300-time steps for both specimens.

Table 4: *Material parameters for the two simulated CLT slabs.*

	CLT slab	
Parameter	Slab1	Slab2
CLT		
E_x, E_y, E_z [GPa]	11, 0.37, 0.37	11, 0.37, 0.37
$\nu_{xy}, \nu_{xz}, \nu_{yz}$ [-]	0, 0, 0	0, 0, 0
G_{xy}, G_{xz}, G_{yz} [GPa]	0.69, 0.345[a], 0.345[a]	0.69, 0.345, 0.345
Radial spring (S4)		
K_o [kN/mm]	[0.5, 0.5, 0.5, 0.5][b]	[0.8, 0.8, 0.8, 0.8]
K_h [N/mm]	[50, 50, 20, 20]	[70, 70, 20, 20]
F_o [kN]	[2.3, 2.3, 1, 1]	[7, 7, 1, 1]
n [-]	[4, 4, 4, 4]	[4, 4, 4, 4]
t_1 [-]	[40, 40][c]	[40, 40]
t_2 [-]	[0.1, 0.1]	[0.1, 0.1]
t_3 [-]	[1, 1]	[1, 1]
J_f [-]	5×10^{-7}	1×10^{-7}
J_k [-]	3×10^{-8}	3×10^{-8}
Gap spring (S1)		
K_g^+ [kN/mm]	2.99	1.74
K_g^- [kN/mm]	74.80	43.56

[a] $G_{xz} = 0.5E_x/(1 + \nu_{xz})$ and $G_{yz} = G_{xz}$; [b] P/N upper and P/N lower values, respectively; and [c] P/N values, respectively.
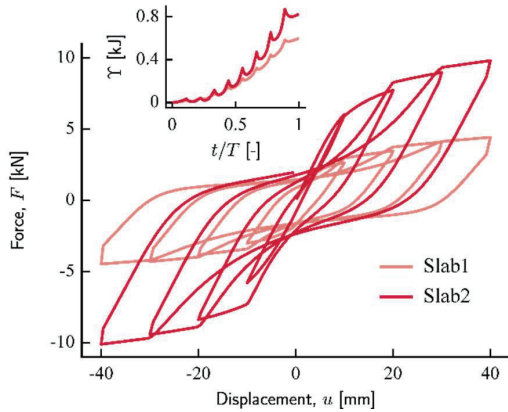
Figure 11: *Force-displacement hysteresis $F(u)$ of the S4 radial fastener spring element for the two simulated CLT slabs. The figure includes the respective dissipated energy-relative time step $Y(t/T)$ relation.*

Figure 11 depicts the force-displacement hysteresis of the S4 spring element (radial fastener) with the RA model for the two simulated CLT slabs. Note that the fastener springs of Slab2 have more strength/stiffness than used in Slab1, which is according to the admissible strength capacity of each screw [19]. The traditional inverse iterative approach is considered to calibrate the parameters of springs S1 and S4 for both specimens, where the force-lateral displacement curve $F_y(u_y)$ of each entire FE model is used to minimize the error concerning the experimental test (see Figure 12). Additional experimental CLT connection tests under monotonic/cyclic axial and in-plane shear loads can be required to directly calibrate the spring elements (S1 and S4) to avoid this iterative process. During this process, it was observed that the tensile gap stiffness of spring S1 plays a key role in the failure mechanism of the entire model, especially at the hardening phase. Small values of this parameter give a more CLT panel rotation, whereas large values generate a quasi-pure panel translation.
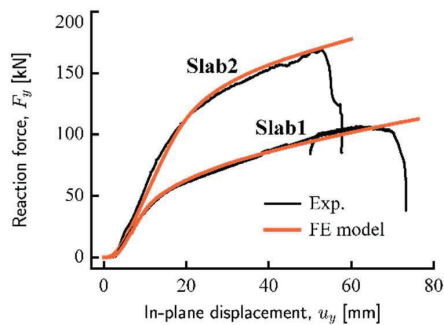

Figure 12: *Comparison of reaction force-displacement $F_y(u_y)$ for the two tested and simulated CLT slabs.*

Figure 12 compares the experimental measurements concerning the reaction force-lateral in-plane displacement $F_y(u_y)$ curve of each simulated CLT slab. It should be noted that for Slab 1, it was necessary to add an offset displacement of 2.5 mm to the experimental data

due to an initial gap separation of 5mm in the model. Nevertheless, it was observed in both slab models a good fit for the elastic and hardening phase concerning experimental results. Although the RA model includes strength degradation, the complete FE model cannot adequately simulate both tests' abrupt softening failure phase.

Figure 13 shows the equivalent von Mises stress (i.e., $\sigma_{eqv} = \sqrt{3/2 s : s}$, with $s = \sigma - (\sigma_x + \sigma_y + \sigma_z)I/3$ is the deviatoric stress tensor and σ is the Cauchy stress tensor) of the two simulated CLT slabs at the final time step. The maximum value of this field in both specimens is observed to be lower than the allowable compressive strength parallel-to-fibre of panels obtained from the current timber code designs, i.e., $f_{c,0}$=8 MPa [20]. Moreover, the images also show the displacement field, which agrees with the failure mechanism of both experimental tests [18].
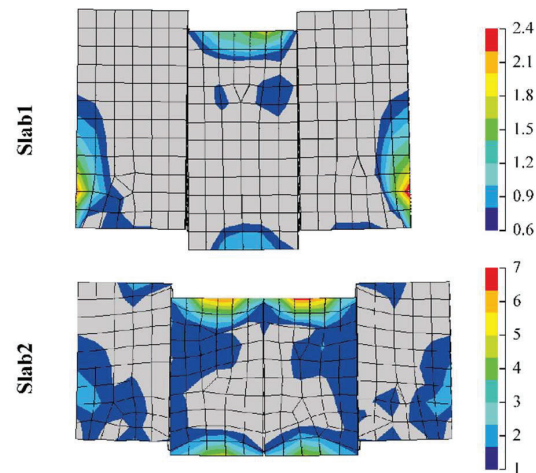

Figure 13: *Equivalent von Mises stress field σ_{eqv} of the two simulated CLT slabs. Units in MPa. Note: the images also include the displacement field amplified by 3 times.*

4 CONCLUSIONS

A new Finite Element (FE) model is proposed to simulate the discrete-fastener panel-to-panel CLT connections. A set of five linear/non-linear uncoupled spring elements are considered, where each of them simulates the main phenomenological effect of connections under different loading conditions: (i) gap of panels with an axial element and asymmetrical tensile/compressive (gap) model; (ii) in-plane and out-of-plane slip of panels with two linear-elastic uniaxial elements; and (iii) radial and out-of-plane bending stiffness/strength capacity of fastener with a respective radial and uniaxial element using both the modified Richard-Abbott hysteretic model. The main conclusions are:

- On one hand, the gap model adequately simulates the axial behaviour (closure/opening) of CLT panels. On the other hand, the modified Richard-Abbott model

predicts well the contribution of discrete fasteners for the CLT connections. In addition, this model accurately simulates the hysteresis of a generic timber connection, including pinching, asymmetric positive/negative loading, and stiffness/strength degradation phenomena.

- The FE connection model simulates three satisfactory loading conditions: axial, in-plane shear, and out-of-plane bending. The gap effect (open/closure) is correctly simulated at axial loads, where a hysteretic tensile/linear compressive regime is stated. Moreover, at in-plane shear loads with a free panel rotation, a snap-trough behaviour at small displacements is observed due to the coupling of gap and radial fastener springs. Also, at bending loads, the pure bending fastener spring is represented in the overall response of the model.

- The FE model is correctly validated with the experimental results of two CLT slabs under in-plane monotonic loads. Furthermore, the 3D FE models generated agree with the experimental tests regarding initial/hardening stiffnesses, strength capacity, and failure mechanism. Also, it is observed that a critical role plays in the tensile stiffness of the gap spring in predicting the failure mechanism of the entire specimen, where smaller values give larger panel rotations.

ACKNOWLEDGEMENT

REFERENCES

[1] Pei S., Rammer D., Popovski M., Williamson T., Line P., van de Lindt J.W.: An overview of CLT research and implementation in North America. In: *14th WCTE*, Vienna, Austria, 2016.

[2] Sullivan K., Miller TH., Gupta R.: Behavior of cross-laminated timber diaphragm connections with self-tapping screws. *Engineering Structures*, 168: 505–524, 2018.

[3] Hossain A., Popovski M., Tannert T.: Cross-laminated timber connections assembled with a combination of screws in withdrawal and screws in shear. *Engineering Structures*, 168: 1–11, 2018.

[4] Gavric I., Fragiacomo M., Ceccotti A.: Strength and deformation characteristics of typical X-lam connections. In: *12th WCTE*, Auckland, New Zealand, 2012.

[5] Gavric I., Fragiacomo M., Ceccotti A.: Cyclic behaviour of typical metal connectors for cross-laminated (CLT) structures. *Materials & Structures*, 48: 1841–1857, 2015.

[6] Rinaldin G., Amadio C., Fragiacomo M.: A component approach for the hysteretic behaviour of connections in cross-laminated wooden structures. *Earthquake Engineering & Structural Dynamics*, 42 (13): 2023–2042, 2013.

[7] Ávila F., Dechent P., Opazo A.: Seismic behaviour evaluation of CLT horizontal diaphragms on hybrid buildings with reinforced concrete shear walls. *Engineering Structures*, 244: 112698, 2021.

[8] D'Arenzo G., Casagrande D., Reynolds T., Fossetti M.: In-plane elastic flexibility of cross laminated timber floor diaphragms. *Construction and Building Materials*, 209: 709–724, 2019.

[9] Pozza L., Saetta A., Savoia M., Talledo D.: Coupled axial-shear numerical model for CLT connections, *Construction and Building Materials*, 150: 568–582, 2017.

[10] Izzi M., Rinaldin G., Fragiacomo M., Polastri A.: Numerical modelling of steel-to-timber joints and connectors for CLT structures. In: *14th WCTE*, Vienna, Austria, 2016.

[11] Stewart WG.: The seismic design of plywood sheated shear walls, Ph.D. thesis, *University of Canterbury*, Christchurch, New Zealand, 1987.

[12] Ismail M., Ikhouane F., Rodellar J., The hysteresis Bouc-Wen model, a survey. *Archives in Computational Methods Engineering*, 16: 161–188, 2009.

[13] Pang WC., Rosowsky D., Pei S, van de Lindt JW.: Evolutionary parameter hysteretic model for wood shear walls. *Journal of Structural Engineering*, 133 (8): 1118–1129, 2007.

[14] Ibarra LF., Medina RA., Krawinkler H.: Hysteretic models that incorporate strength and stiffness deterioration. *Earthquake Engineering & Structural Dynamics*, 34: 1489–1511, 2005.

[15] Chacón MF., Guindos P., Montaño, Jara A., Benedetti F., Lagos J., Veliz F. Finite element formulation for modelling cross-laminated timber diaphragm connections. Submitted to *Construction and Building Materials*, 2023.

[16] ANSYS. ANSYS Academic Research, Release 20.0, *ANSYS, Inc.*, Canonsburg, Pennsylvania, 2022.

[17] Nogueiro P., da Silva LS., Bento R., Simões R. Numerical implementation and calibration of a hysteretic model with pinching for the cyclic response of steel and composite joints. *Advances in Steel Structures*, 1: 767–774, 2005.

[18] Veliz F., Guindos P., Montaño J., Lagos J.: Experimental monotonic in-plane behavior of high-capacity light-frame and cross-laminated timber diaphragms. Submitted to *Engineering Structures*, 2023.

[19] Strong-Tie S. Fastening Systems Technical Guide. *Simpson Strong-Tie Company Inc.*, Canada, 2023.

[20] NCh1198. Wood–Wood Construction–Calculation (in Spanish). *Instituto Nacional de Normalización*. Santiago, Chile, 2014.